

# Evaluation of Rare-Earth Modified ZrB<sub>2</sub>–SiC Ablation Resistance Using an Oxyacetylene Torch

Winnie Tan, Mitchell Adducci, and Rodney Trice<sup>†</sup>

Purdue University, West Lafayette, Indiana 47907

Rare-earth modified ZrB<sub>2</sub>–SiC coatings were prepared via mechanical mixing Sm<sub>2</sub>O<sub>3</sub> or Tm<sub>2</sub>O<sub>3</sub> powders with spray-dried ZrB<sub>2</sub>, or by chemically doping samarium ions into spray-dried ZrB<sub>2</sub>. In either approach, SiC powders were also added and coatings were fabricated via shrouded air plasma spray. An oxyacetylene torch was utilized to evaluate the coatings under high heat flux conditions for hold times of 30 and 60 s. The resulting phases and microstructures were evaluated as a function of rare-earth type, modification approach, and ablation time. A brittle *m*-ZrO<sub>2</sub> scale was observed in the ZrB<sub>2</sub>/SiC-only coating after ablative tests; during cooling this scale detached from the unreacted coating. In contrast, rare-earth modified coatings formed a protective oxide scale consisting primarily of either Sm<sub>0.2</sub>Zr<sub>0.8</sub>O<sub>1.9</sub> or Tm<sub>0.2</sub>Zr<sub>0.8</sub>O<sub>1.9</sub>, along with small amount of *m*-ZrO<sub>2</sub>. These rare-earth oxide scales displayed high thermal stability and remained adhered to the unreacted coating during heating and cooling, offering additional oxidation protection.

## I. Introduction

DESIGN of next generation hypersonic vehicles involves employing sharp leading edges and nose tips, where the radii are on the order of a few millimeters.<sup>1</sup> These designs improve vehicle maneuverability, safety, and performance. However, the sharp features increase the convective heating experienced at these leading edges, resulting in surface temperatures exceeding 2000°C.<sup>1–3</sup> Ultra high-temperature ceramics (UHTCs) are expected to perform in these extreme environments of high temperature, chemical reactivity, erosion attacks, and more.<sup>4</sup> One promising UHTC is ZrB<sub>2</sub>/SiC.<sup>3,5,6</sup> Although these individual materials have melting temperatures above 2000°C, their exposure to oxidizing environments causes degradation, limiting their operating temperature to ~1600°C. As oxidation of the ZrB<sub>2</sub>/SiC is inevitable, research efforts have focused on improving its oxidation properties via the addition of different compounds to promote densification of the zirconia scale and to reduce the evaporation of the borosilicate glass.<sup>7–10</sup>

In addition to improving the high-temperature properties of a UHTC, it may also be possible to increase dissipation of heat in leading edges and other hot structures by increasing surface emissivity, hence increasing radiation heat transfer.<sup>11</sup> For instance, a mathematical model proposed by Van Wie *et al.*<sup>11</sup> demonstrated that under an identical heat flux the wall temperature of a hypersonic vehicle is reduced by 300°C when its surface emissivity is increased from 0.5 to 1.0 at Mach 10. Prior studies from the 1960s and 1970s indicate that some rare-earth oxides possess high values of emissivity

over ultraviolet and near infrared wavelengths of 0.6–2 μm.<sup>12,13</sup> The partially occupied *f*-electron shell of samarium and thulium contributes to this high emittance.<sup>14</sup> Recent studies at 1200°C demonstrated an increase in total hemispherical emissivity of samarium-doped ZrB<sub>2</sub>/SiC coatings from 0.8 to 0.93 compared to ZrB<sub>2</sub>/SiC coatings.<sup>15</sup> However, it is not clear how the rare-earth modified ZrB<sub>2</sub>/SiC coatings will perform in high heat flux environments that are typical of hypersonic flight.

In this work, the ZrB<sub>2</sub>/SiC coatings were modified by attempting to incorporate 10 mol.% Sm<sub>2</sub>O<sub>3</sub>, 10 mol.% Tm<sub>2</sub>O<sub>3</sub>, or 20 mol.% Sm(NO<sub>3</sub>)<sub>3</sub> into the final coating. The specimens were exposed to an oxyacetylene torch and rapidly heated to temperatures in excess of 1900°C. The microstructures and phase assemblage after ablative tests were investigated and discussed. This work aims to understand the effects of different rare-earth modifiers on the ablative properties of the plasma-sprayed ZrB<sub>2</sub>/SiC coatings.

## II. Experimental Procedure

### (1) Starting Materials, Rare-Earth Modification, and Coating Fabrication

An overview of the as-prepared coating formulations studied is listed in Table I. ZrB<sub>2</sub> (1.5–3.0 μm; HC Starck, Munich, Germany) was spray dried to create powder agglomerates with a *d*<sub>50</sub> of ~38 μm. Two types of mixing approaches were investigated to incorporate rare-earth oxides or ions into the final coating: dry-mixing (DM) and chemical-doping (DOP). In the DM approach, spray dried ZrB<sub>2</sub>, SiC (0.7 μm; HC Starck), and 10 mol.% of either Sm<sub>2</sub>O<sub>3</sub> or Tm<sub>2</sub>O<sub>3</sub> powders (99.9% pure; American Elements, Los Angeles, CA) were dry-mixed and roller milled to ensure homogeneous mixing. In the DOP approach, 20 mol.% samarium nitrate, Sm(NO<sub>3</sub>)<sub>3</sub> (99.9% pure; Sigma-Aldrich, St. Louis, MO) was dissolved in 200-proof ethanol and infiltrated into spray-dried ZrB<sub>2</sub> agglomerates. The suspension was dried with a rotating evaporator, followed by a heat treatment at 500°C in air for 1 h to remove residual moisture and nitrates. The dried agglomerate was sieved using a 325-mesh (≤44 μm) and 20 vol.% SiC was mechanically mixed into the Sm(NO<sub>3</sub>)<sub>3</sub> infiltrated ZrB<sub>2</sub> powder. Both the DM and DOP powder compositions contained 0.5 wt.% fumed silica (Cab-O-Sil<sup>®</sup>; Cabot Corporation, Boston, MA) to improve the flow of powders into the plasma plume. The coatings were prepared at Praxair Surface Technologies (Indianapolis, IN) using a proprietary shrouded air plasma spray process that allowed plasma spraying at atmospheric pressures in an inert environment without oxidation of the ZrB<sub>2</sub> or SiC powders.<sup>15</sup> All coatings were deposited on 6.35 mm thick Al<sub>2</sub>O<sub>3</sub> substrates. The Al<sub>2</sub>O<sub>3</sub> has coefficient of thermal expansion (CTE) of 7–8 × 10<sup>–6</sup>°C<sup>–1</sup>, which is lower than *m*-ZrO<sub>2</sub> (~8.4 × 10<sup>–6</sup>°C<sup>–1</sup>).<sup>16,17</sup>

The following naming sequence is used to simplify the discussion: rare-earth type followed by the baseline composition–mixing method. The baseline coating (ZrB<sub>2</sub>/SiC) was identified as ZBS and a SmZBS-DM coating consisted of Sm<sub>2</sub>O<sub>3</sub>, spray-dried ZrB<sub>2</sub> and SiC powders, with the Sm<sub>2</sub>O<sub>3</sub>

W. Fahrenholtz—contributing editor

**Table I. As-Prepared Chemical Formulations, Actual Coating Compositions, and Physical Properties of As-Sprayed Coatings Fabricated via Shrouded Air Plasma Spray**

	Sm <sub>2</sub> O <sub>3</sub> (mol. %)	Tm <sub>2</sub> O <sub>3</sub> (mol. %)	Sm(NO <sub>3</sub> ) <sub>3</sub> (mol. %)	Actual Sm/Tm (mol. %)	Theoretical Density <sup>†</sup> (g/cm <sup>3</sup> )	Bulk Density (g/cm <sup>3</sup> )	Porosity (%)
ZBS	—	—	—	—	6.07	4.30	29.1
SmZBS-DM	10.0	—	—	15.1	6.44	4.68	27.3
TmZBS-DM	—	10.0	—	15.1	6.46	4.91	24.0
SmZBS-DOP	—	—	20.0	7.4	5.74	3.35	41.4

<sup>†</sup>All coatings formulation contained ZrB<sub>2</sub>-20 vol.% SiC powder. Deposition efficiency varies from the formulation due to powder flow properties and incorporation method. Actual as-sprayed coatings contained ~1.7 vol.% of SiC in all coatings. Theoretical density calculations were performed based on the as-sprayed coatings composition.

added via the dry-mixed approach. The thicknesses of the ZBS, SmZBS-DM, TmZBS-DM, and SmZBS-DOP coatings were approximately 167, 212, 241, and 197 μm, respectively.

### (2) Oxyacetylene Ablative Test

A series of ablative tests were performed to evaluate and compare the ablation resistance of the coatings in dynamic heating conditions. The oxyacetylene ablative test setup was constructed using ASTM 285-08<sup>18</sup> as a standard. Figure 1 shows a schematic of the setup. A two-color pyrometer (OS3750; Omega Engineering Inc., Stamford, CT) and a type-K thermocouple were used to measure the front and back face temperatures, respectively. Each was also connected to a data logger to record the temperatures as a function of time. The two-color pyrometer has the capability of measuring surface temperatures between 400°C and 3000°C. The emissivity of the pyrometer was set to 0.9 for all coatings because the emissivity of each coating in oxidizing conditions was not known. While emissivity measurements have been made on similar coatings to those studied currently, those measurements were made in a vacuum and thus did not form any oxide scale.<sup>15</sup> The coatings were sectioned into 25.4 mm × 25.4 mm square specimens and were held by two pieces of graphite in the fixture. The ablation torch (Victor Technologies, St. Louis, MO) had a 3 mm orifice and the separation distance between specimen and torch was held constant at 20 mm. An oxygen-rich flame with a 10:12 slpm acetylene to oxygen ratio, also held constant for each test, was used to simulate the oxidizing operating environment. The flow rates were controlled by two separate digital flow meters with an accuracy of 0.1 slpm. Specimens were tested for 30 or 60 s, with time beginning when the flame first hit the specimen surface. The duration of each test was monitored manually. The oxyacetylene torch heating rate was ~167 ± 3°C/s over the first 10 seconds of testing. After 30 s, the ZBS, SmZBS-DM, TmZBS-DM, and SmZBS-DOP coatings exhibited temperatures of 2027°C, 2039°C, 2026°C, and 1931°C. The higher surface temperatures measured for the first three coatings, as compared to the surface temperature measured for the rare-earth-doped coatings, suggested that the SmZBS-DOP coating has a higher emissivity. Furthermore, all measured surface temperatures would be an underestimation of the actual surface temperature if the emissivity of the evolving oxide scale is <0.9. The mass change that occurred during ablation testing was not reported in this study because the alumina substrate cracked off during testing due the thermal shock.

### (3) Phase and Microstructural Analysis

X-ray diffraction (XRD) using CuK<sub>α</sub> radiation (D8 Focus; Bruker Corporation, Billerica, MA) was performed on as-sprayed and postablative tested coatings at 2θ values of 20°–50°. A step size of 0.02° and a scan rate of 5°/min were used. The density of the coatings was determined using

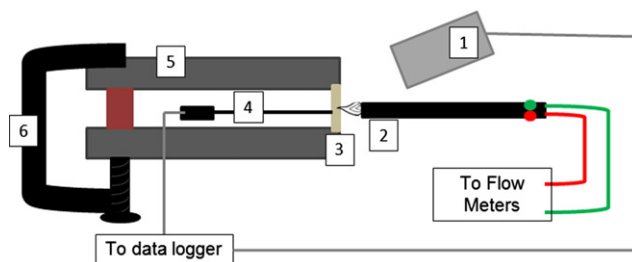


**Fig. 1.** Schematic of ablation test setup with reference to ASTM E285-08. The setup consisted of (1) two-color optical pyrometer, (2) oxyacetylene torch, (3) specimen, (4) back-face thermocouple, (5) specimen holder, and (6) c-clamp. Both the pyrometer and thermocouple were connected to a data logger to record temperatures.

Archimedes methodology described in the ASTM C373-88.<sup>19</sup> The theoretical density was calculated using the rule of mixtures approach based on final coating compositions, where the density of ZrB<sub>2</sub>, SiC, Sm<sub>2</sub>O<sub>3</sub>, and Tm<sub>2</sub>O<sub>3</sub> are 6.09, 3.21, 8.35, and 8.60 g/cm<sup>3</sup>, respectively. For the SmZBS-DOP coatings, the density of samarium, 7.52 g/cm<sup>3</sup> was used as an estimate. Coating topography and cross-sectional micrographs were observed using a scanning electron microscope (SEM) equipped with energy-dispersive X-ray spectroscopy (EDS) (Phillips XL-40; FEI Co., Hillsboro, OR). The cross-sectioning and polishing processes were performed with a nonaqueous media. The nonconductive ceramic coatings were coated with a thin layer of Au/Pd prior to imaging.

## III. Results

### (1) As-Sprayed Coatings

The theoretical and bulk densities, and porosity of the as-sprayed coatings are listed in Table I. Figures 2(a) and (b) show the topography and cross-sectional view of the ZBS coating, which was also typical for the DM coatings, but not for the SmZBS-DOP coating as shown in Figs. 2(c) and (d). The ZrB<sub>2</sub> and SiC powder in the SmZBS-DOP coating was partially melted; therefore, the coating was more porous compared to the rest of the coatings. A more complete description of the coating microstructures is reported in Ref. [15].

The crystalline phases of the as-sprayed coatings detected via XRD are summarized in Table II. A small amorphous hump associated with the added SiO<sub>2</sub> flowing agent was observed in all coatings. Furthermore, the primary peaks of all coatings were attributed to ZrB<sub>2</sub>, with only small SiC peaks observed at 2θ = 35.5°. The appearance of peaks associated with rare-earth oxides in the DM coatings indicates successful incorporation of these compounds into to the ZrB<sub>2</sub>/SiC coatings. Though the samarium dopant in SmZBS-DOP was not detected in the XRD, 7.4 mol.% Sm was identified by mass spectroscopy.<sup>15</sup> Note that this concentration

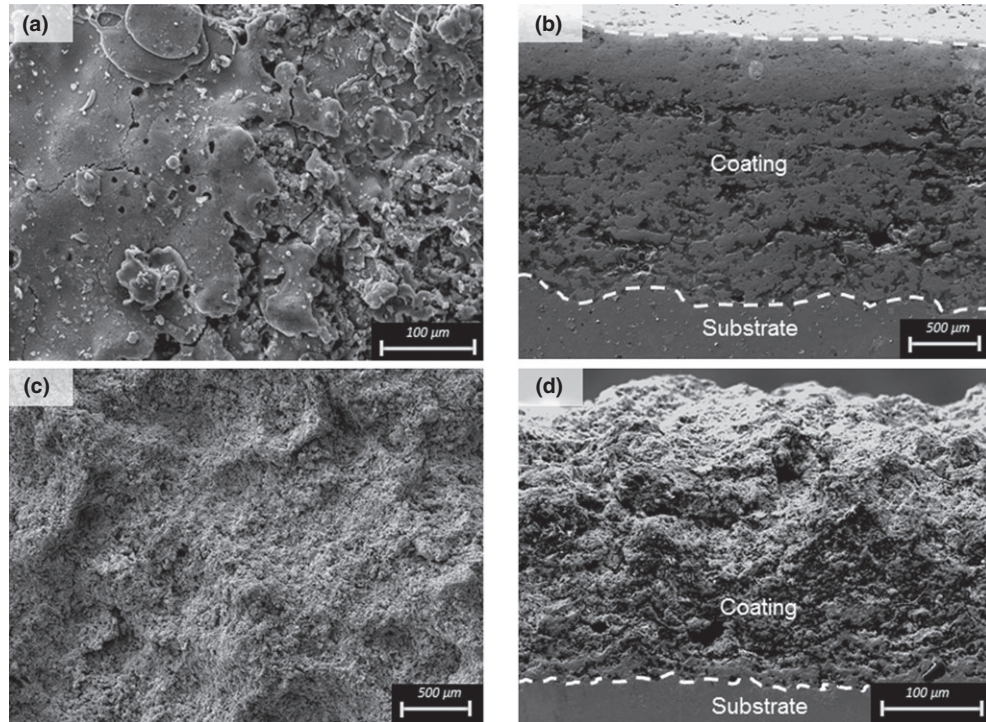


**Fig. 2.** The as-sprayed ZBS coating consisted of an accumulation of splats, with (a) topography and (b) cross-sectional micrographs revealing the typical microstructure of the shrouded air-plasma-sprayed coatings. The as-sprayed SmZBS-DOP coating was more porous, with (c) topography and (d) cross-sectional micrographs showing powders that were partially melted during the plasma spray process.

**Table II.** Phases Present on the Surface of As-Sprayed Coatings and After Ablation Testing (30 and 60 s) as Identified by XRD

	As-sprayed	30 s	60 s
ZBS	ZrB <sub>2</sub> +α-SiC	<i>m</i> -ZrO <sub>2</sub> +ZrB <sub>2</sub>	<i>m</i> -ZrO <sub>2</sub> +ZrB <sub>2</sub>
SmZBS-DM	ZrB <sub>2</sub> +α-SiC+Sm <sub>2</sub> O <sub>3</sub>	Sm <sub>0.2</sub> Zr <sub>0.8</sub> O <sub>1.9</sub> + <i>m</i> -ZrO <sub>2</sub>	Sm <sub>0.2</sub> Zr <sub>0.8</sub> O <sub>1.9</sub> + <i>m</i> -ZrO <sub>2</sub>
TmZBS-DM	ZrB <sub>2</sub> +α-SiC+Tm <sub>2</sub> O <sub>3</sub>	Tm <sub>0.2</sub> Zr <sub>0.8</sub> O <sub>1.9</sub> + <i>m</i> -ZrO <sub>2</sub>	Tm <sub>0.2</sub> Zr <sub>0.8</sub> O <sub>1.9</sub> + <i>m</i> -ZrO <sub>2</sub>
SmZBS-DOP	ZrB <sub>2</sub> +α-SiC <sup>†</sup>	Sm <sub>0.2</sub> Zr <sub>0.8</sub> O <sub>1.9</sub> + <i>m</i> -ZrO <sub>2</sub> +ZrB <sub>2</sub> +SiC	Sm <sub>0.2</sub> Zr <sub>0.8</sub> O <sub>1.9</sub> + <i>m</i> -ZrO <sub>2</sub>

<sup>†</sup>7.4 mol% Sm was detected in this coating via ICP mass spectroscopy.

was much less than the 20 mol.% Sm added initially to the spray-dried ZrB<sub>2</sub> powders.

### (2) Phases Analysis Post-ablative Testing

The major constituent phases as determined by XRD in each of the coatings after ablative testing are summarized in Table II. After the 30 s ablative test, an amorphous hump was observed in all XRD patterns at  $2\theta$  between 10° and 22°. The presence of an amorphous hump at low  $2\theta$  for all ablated coatings was consistent with previous studies of oxidation on ZrB<sub>2</sub>/SiC materials. Generally, this is attributed to the presence of B<sub>2</sub>O<sub>3</sub>, SiO<sub>2</sub> or borosilicate glassy phases.<sup>5,6</sup> The ZBS surface consisted mainly of *m*-ZrO<sub>2</sub>. After the 30 and 60 s tests, only a trace amount of *m*-ZrO<sub>2</sub> was detected in the coatings in the rare-earth modified coatings. A cubic structure (fluorite), either *c*<sub>1</sub>-Sm<sub>0.2</sub>Zr<sub>0.8</sub>O<sub>1.9</sub> or *c*<sub>1</sub>-Tm<sub>0.2</sub>Zr<sub>0.8</sub>O<sub>1.9</sub>, was the primary phase in the samarium- and thulium-modified coatings, respectively. Peaks associated with ZrB<sub>2</sub> were detected in the ZBS and SmZBS-DOP coatings. However, we believe these peaks were associated with regions in these samples that were not ablated, therefore not covered with the oxide scale. The small amount of α-SiC observed in all the as-sprayed coatings was only present in the SmZBS-DOP coating after the 30 s test. There was no change in the phases observed in the ZBS, SmZBS-DM, or TmZBS-DM coatings after 60 s compared to those tested for 30 s. After the 60 s test, *c*<sub>1</sub>-Sm<sub>0.2</sub>Zr<sub>0.8</sub>O<sub>1.9</sub> and a trace amount of *m*-ZrO<sub>2</sub> were detected in the SmZBS-DOP coating.

### (3) Surface Features Post-ablative Testing

(A) *General Observations:* The surface topographies and corresponding cross sections for all coatings after 30 and 60 s ablative tests are shown in Fig. 3. For discussion, the surface features are divided into three regions: region I, region II, and region III. These regions are indicated on the ZBS coating in Fig. 3(a). Region I represents the area outside of the ablation zone, where little or no surface oxide was observed. Region II is deemed the ablation zone, representing the region in the specimen where the temperature was the highest and the most severe damage occurred. There was a ~3 mm diameter area in the center of each specimen that experienced less ablation is designated region III. This 3 mm feature was observed in a separate test on a graphite substrate, and was thus attributed to the design of the oxy-acetylene torch tip. The effects of ablation were relatively uniform within region II. All SEM analysis on cross sections was performed in region II and these images are presented in Figs. 3(e)–(h) and (m)–(o). The dark contrast in the top area of each cross section is the epoxy mounting material, followed by the lighter oxide scale and unreacted coating. The two distinctive features of the post-ablative test coatings were as follows: (1) a porous oxide scale on the top surface; and (2) the unreacted coating located between the oxide scale and the substrate. The unreacted coating layer lost its typical thermal spray microstructure after the test, with no individual lamella visible due to sintering.<sup>20</sup>

(B) *Baseline ZBS Coating Scale:* The oxidized scale of the ZBS coatings was brittle and did not adhere com-

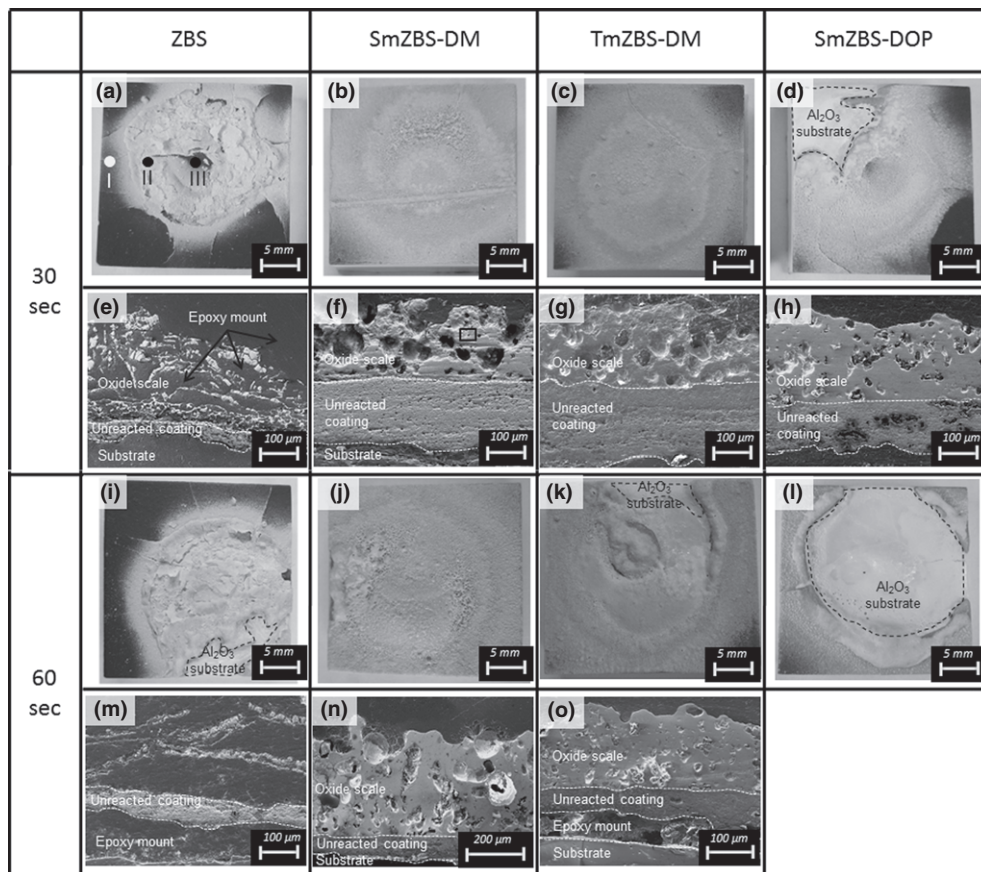


**Fig. 3.** Surface morphology [(a)–(d), (i)–(l)] and corresponding cross-sectional micrographs [(e)–(h), (m)–(o)] in the ablation zone (region II) of all test specimens after a 30 and 60 s ablative test. The dark region of the surface topography is the unoxidized  $ZrB_2/SiC$  coating and the light region is the oxide scale formed in the ablation zone. The area enclosed within the dashed line shows where coatings delaminated during the ablative test. Note that the area enclosed in image (f) is further discussed in Fig. 4 and that the cross-sectional micrograph of image (n) has  $1.5 \times$  higher magnification compared to other cross-sectional micrographs.

pletely to the unreacted coating, resulting in partial detachment of the oxide scale primarily during the cooling cycle after 30 and 60 s tests [see Figs. 3(a) and (i)]. XRD of region II of the coating showed it to be  $m\text{-ZrO}_2$ . Based on previous studies, the amorphous hump observed in the XRD data was the glassy  $SiO_2$ ,  $B_2O_3$  or combination of both.<sup>5,6</sup> The glasses were continuously released into the oxide scale by the ongoing oxidation of the  $ZrB_2/SiC$ . Both the 30 and 60 s cross sections show numerous thin layers of  $m\text{-ZrO}_2$  scale partially detached from the unreacted coating. This delicate microstructure was preserved by flowing epoxy onto the coating surface before any sample handling occurred. Significant amounts of the mounting epoxy reside between the oxide flakes in the cross sections shown in Figs. 3(e) and (m).

**(C) Rare-Earth Modified Coatings Scale:** The surface topographies of the SmZBS-DM and TmZBS-DM coatings were similar, but distinctively different than the ZBS coating. The oxide scale in region II remained intact with the unreacted coating and was significantly denser ( $\sim 50\%$ – $65\%$  dense) compared to the scale observed in the ZBS coating ( $\sim 20\%$ – $30\%$  dense). Regions I and II in the DM coatings were compact and glossy, indicating the presence of surface glass. Figures 3(b) and (c) show a topography in region II consistent with the formation of shallow craters directly below the flame. These craters appear deeper after a 60 s test as shown in Figs. 3(j) and (k). The presence of craters in region II indicates that the glassy phase formed during the ablative test was of low enough viscosity to be displaced by the high gas flow rate (22 slpm) of the torch. As shown in Figs. 3(f) and (g), cross-sectional images of the SmZBS-DM and TmZBS-DM oxide scales contained 5–60  $\mu m$  diameter pores, but appear locally dense between the pores. Figure 4 is a higher

magnification of the SmZBS-DM scale in the dense region between the pores. EDS analysis was used to identify the compositions in region A and region B, with boron being undetectable. The ratios of each element suggested that region A is the  $c_1\text{-Sm}_{0.2}\text{Zr}_{0.8}\text{O}_{1.9}$  phase as detected by XRD. Region B shows a unique “eutectic-like” phase, where multiple layers of glassy and solid phases were embedded within the  $c_1\text{-Sm}_{0.2}\text{Zr}_{0.8}\text{O}_{1.9}$  matrix. Monteverde *et al.*<sup>21</sup> have identified this microstructure previously in a  $ZrB_2/SiC+LaB_6$  composite after an arc-jet test and referred to this feature as a glass separation cluster or GS. The elemental analysis indicates a samarium and silica-rich structure within the GS cluster. With an EDS resolution of 1–2  $\mu m$  and an average GS cluster size of 2–6  $\mu m$ , the GS composition reported in Fig. 4 likely includes signal from the adjacent  $c_1\text{-Sm}_{0.2}\text{Zr}_{0.8}\text{O}_{1.9}$  matrix. The darker contrast regions are likely to be silica rich because of its low atomic number with respect to zirconium. Similar microstructural features including  $c_1\text{-Tm}_{0.2}\text{Zr}_{0.8}\text{O}_{1.9}$  and GS clusters were observed in the TmZBS-DM coating.

Similar oxide scale features were observed in the SmZBS-DOP coating compared to those observed in the SmZBS-DM coating. Region I and II in the SmZBS-DOP coating were glossy, with less apparent craters formed after the 30 s test. As shown in Fig. 3(d), the oxide scale formed by the SmZBS-DOP coating remained adhered to the unreacted coating during heating and cooling. However, partial and full coating delamination (as opposed to oxide scale spallation) was observed after 30 and 60 s tests, respectively. The delaminated and ablated areas for both the 30 and 60 s tests are indicated by the dashed line in Figs. 3(d) and (l). It is not clear why the DOP coating delaminated and the DM coatings did not, but it may be related to the high porosity in the

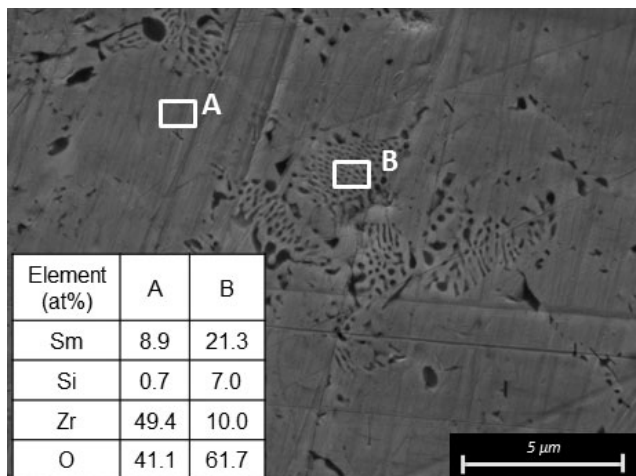


**Fig. 4.** Micrograph of the dense oxide scale in SmZBS-DM after a 30 s ablative test [taken from area enclosed in the white box of Fig. 3(f)]. The elemental analysis of the  $\text{Sm}_{0.2}\text{Zr}_{0.8}\text{O}_{1.9}$  matrix (region A) and the glass separation cluster (region B) are shown in the table.

as-sprayed DOP coating. This points to the need to optimize the plasma spray parameters for the SmZBS-DOP coatings. The cross-sectional view of the 30 s SmZBS-DOP coating [Fig. 3(h)] was similar to that of SmZBS-DM and TmZBS-DM coatings such that the oxide scale was locally dense with pores dispersed in the coating. However, no GS microstructure was observed, possibly due to having less  $\text{Sm}^{3+}$  in this coating.

(D) *Comparison of Ablation Resistance:* As evidenced by the thickness of the unreacted coating, the oxide scales formed by the rare-earth modified coatings provided greater ablation protection compared to the  $m\text{-ZrO}_2$  scale formed by the ZBS coating. Measurements of the unreacted thickness for each coating after the 30 s test revealed that  $\sim 80\%$  of the original coating thickness for rare-earth modified coatings remained. In contrast, only  $\sim 30\%$  of the unreacted ZBS coatings remained. Whether the starting porosity influenced this result was considered. As previously presented in Table I, the total porosity of all the as-sprayed coatings studied presently ranged between 24% and 42%. The porosity was highest for the SmZBS-DOP coating and lowest for the ZBS coating. However, the ablation resistance of the SmZBS-DOP was better than that of the ZBS coating due to the nature of the oxide scale formed. Though the high porosity in the SmZBS-DOP coating may have influenced its ability to stay adhered to the underlying substrate.

#### IV. Discussion

##### (1) ZBS Oxide Scale

The flaky oxide scale observed in the ZBS coatings after either a 30 or 60 s test [Figs. 3(e) and (m)] is not generally observed in furnace oxidized  $\text{ZrB}_2/\text{SiC}$  UHTCs densified via traditional powder processing routes.<sup>5,6,22</sup> The  $\text{ZrB}_2$  grains in these sintered composites are usually equiaxed. After oxidation, equiaxed  $\text{ZrO}_2$  grains surrounded by  $\text{SiO}_2\text{-B}_2\text{O}_3$  glassy phase are observed in the scale. The as-sprayed ZBS coatings, on the other hand, are comprised of stacked lamellae with low adhesion between the lamellae due to the significant amounts of interlamellar porosity. Thus, it would be expected that the interlamellae adhesion in plasma-sprayed coatings would be less than the intergranular adhesion in a densified  $\text{ZrB}_2/\text{SiC}$  UHTC. During the ablative test, the low thermal conductivity of the zirconia and thermal shock from the high heat flux may cause layers of lamellae to detach from the underlying coatings as observed in Figs. 3(e) and (m). The average thickness of lamella in

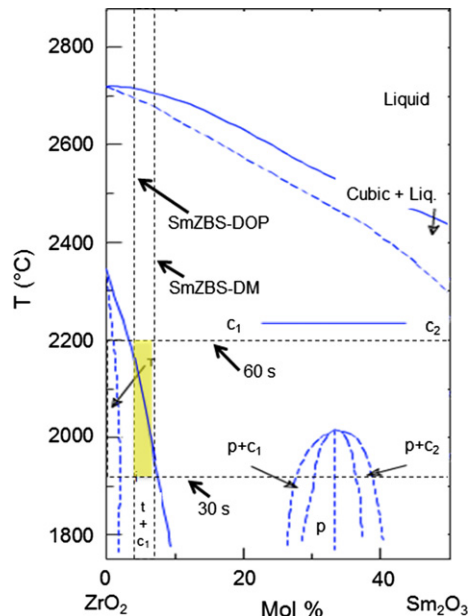


**Fig. 5.** The  $\text{ZrO}_2\text{-Sm}_2\text{O}_3$  phase diagram, adapted from Ref. [23], in the high-temperature region. The vertical lines along the composition axis correspond to the amount of  $\text{Sm}_2\text{O}_3$  in the as-sprayed SmZBS-DOP and SmZBS-DM coatings, respectively, whereas the horizontal lines represent estimated test temperatures during ablation testing. The box defined by the composition and temperature limits represents the expected phases to form as a function of coating composition and test temperature. The  $t$  and  $c_1$  are  $t\text{-ZrO}_2$  and  $c_1\text{-Sm}_{0.2}\text{Zr}_{0.8}\text{O}_{1.9}$  solid solution, respectively.

the ZBS coating was  $\sim 3.1\ \mu\text{m}$  compared to the average thickness of the  $m\text{-ZrO}_2$  oxide flakes of  $\sim 5.5\ \mu\text{m}$ . It is possible that multiple layers of lamellae detached simultaneously to form a single flake, exposing the unreacted coating and causing continuous consumption of the coatings during the ablation process.

##### (2) Phase Assemblage in Rare-Earth Modified Coatings

In prior static furnace tests on ZBS coatings in air, the oxide scale formed after 2 h at  $1300^\circ\text{C}$  was comprised of only  $m\text{-ZrO}_2$ .<sup>15</sup> When exposed to identical conditions rare-earth modified coatings were also comprised of only  $m\text{-ZrO}_2$  scale. At these low oxidation temperatures ( $\sim 1300^\circ\text{C}$ ), the presence of the rare-earth ions had no beneficial effect in terms of oxidation resistance as compared to the ZBS coatings. In contrast, this study suggests that coatings modified with rare-earth oxides or ions demonstrate superior ablation resistance compared to the ZBS coatings in the  $1930^\circ\text{C}\text{-}2200^\circ\text{C}$  range investigated.

The improvement in ablation performance of the rare-earth modified coatings is attributed to the “*in situ*” formation of a refractory oxide, mainly  $c_1\text{-Sm}_{0.2}\text{Zr}_{0.8}\text{O}_{1.9}$  or  $c_1\text{-Tm}_{0.2}\text{Zr}_{0.8}\text{O}_{1.9}$ . There is  $\sim 7.6\ \text{mol.}\%$   $\text{Sm}_2\text{O}_3$  in the as-sprayed SmZBS-DM coating and  $\sim 3.7\ \text{mol.}\%$   $\text{Sm}_2\text{O}_3$  in the SmZBS-DOP coating, assuming all the added  $\text{Sm}^{3+}$  ions have oxidized. The concentrations of  $\text{Sm}_2\text{O}_3$  present in the SmZBS-DM and SmZBS-DOP coatings are marked by the vertical lines in the  $\text{ZrO}_2\text{-Sm}_2\text{O}_3$  phase diagram in Fig. 5 adapted from Ref. [23]. The estimated high and low temperatures that occur during ablation testing are also marked on the phase diagram via the two horizontal lines. Within the highlighted box in Fig. 5(a) cubic structure, identified as  $c_1\text{-Sm}_{0.2}\text{Zr}_{0.8}\text{O}_{1.9}$ , is predicted to form, consistent with the XRD results presented in Table II. Within the two-phase region of the phase diagram enclosed by the highlighted box, a  $t\text{-ZrO}_2$  phase would also be expected. This phase was not observed in XRD measurements performed at room temperature,

because the  $t$ -ZrO<sub>2</sub> is expected to transform to  $m$ -ZrO<sub>2</sub> upon cooling, consistent with the results in Table II. Analogous to the SmZBS-DM coatings,  $c_1$ -Tm<sub>0.2</sub>Zr<sub>0.8</sub>O<sub>1.9</sub> was observed in the TmZBS-DM coating after ablative testing. The Tm<sub>2</sub>O<sub>3</sub>-ZrO<sub>2</sub> phase diagram available in literature<sup>24</sup> is unlabeled, however, there is considerable similarity with the Sm<sub>2</sub>O<sub>3</sub>-ZrO<sub>2</sub> phase diagram in the zirconia-rich region.

### (3) Pore Formation in the Rare-Earth Modified Coatings

The rare-earth modified coating cross sections [Figs. 3(f)–(h), (n) and (o)] shows the presence of micrometer-sized pores in the oxide scales which were not observed in the ZBS oxide scale. The spherical nature of the pores suggests the possible formation of a liquid phase during oxidation that eventually volatilized as the local temperature exceeded the evaporation temperature.<sup>22</sup> This liquid phase is known to be the B<sub>2</sub>O<sub>3</sub>, SiO<sub>2</sub>, or a combination of both, formed during the oxidation of ZrB<sub>2</sub>/SiC UHTCs. As B<sub>2</sub>O<sub>3</sub> volatilizes at temperatures above 500°C, the large pores observed in Figs. 3(f)–(h), (n) and (o) could be attributed to the volatility of gaseous by-products such as B<sub>2</sub>O<sub>3</sub>, BO<sub>2</sub>, and BO.<sup>25</sup> Pores with similar size and shape were also observed in Refs. [21] and [26] for ZrB<sub>2</sub>/SiC UHTCs. These gaseous products could escape via the highly porous interconnected porosity in the ZBS coatings.

### (4) Oxide Scale Adherence in the Rare-Earth Modified Coatings

It is worth noting that in this study the oxide scale formed by the rare-earth modified coatings (primarily  $c_1$ -Sm<sub>0.2</sub>Zr<sub>0.8</sub>O<sub>1.9</sub> or  $c_1$ -Tm<sub>0.2</sub>Zr<sub>0.8</sub>O<sub>1.9</sub>) adhered to the unreacted coatings during cooling, whereas the oxide scale formed by the ZBS coating (primarily  $m$ -ZrO<sub>2</sub>) did not. Consideration of the CTE of each component reveals similar expansion behavior. For instance, the CTE of ZrB<sub>2</sub>,  $m$ -ZrO<sub>2</sub> and Sm<sub>0.2</sub>Zr<sub>0.8</sub>O<sub>1.9</sub> is  $\sim 6.8$ – $8.4 \times 10^{-6} \text{C}^{-1}$ ,  $\sim 8.4 \times 10^{-6} \text{C}^{-1}$ , and  $\sim 7.7 \times 10^{-6} \text{C}^{-1}$ , respectively.<sup>16,17,27</sup> Although it is true that  $m$ -ZrO<sub>2</sub> has a relatively similar CTE to ZrB<sub>2</sub>, there is a  $t$ - to  $m$ -ZrO<sub>2</sub> phase transformation that occurs in all the coatings currently evaluated upon cooling at  $\sim 950^\circ\text{C}$ .<sup>28</sup> The resulting 3%–5% volume expansion associated with this phase transformation can locally alter the state of stress, and its affect should be proportional to its volume fraction in the oxide scale. As shown in Table II,  $c_1$ -Sm<sub>0.2</sub>Zr<sub>0.8</sub>O<sub>1.9</sub> or  $c_1$ -Tm<sub>0.2</sub>Zr<sub>0.8</sub>O<sub>1.9</sub> and only a trace amount of  $m$ -ZrO<sub>2</sub> were detected in all the rare-earth modified coatings after 30 and 60 s tests. Thus, the  $t$ - to  $m$ -ZrO<sub>2</sub> transformation appears to have not caused delamination of this oxide scale. In the ZBS coating,  $m$ -ZrO<sub>2</sub> was the only phase detected in the oxide scale and its transformation from  $t$ -ZrO<sub>2</sub> caused spallation during cooling.

## V. Summary and Conclusions

Oxyacetylene ablative tests were performed on baseline ZrB<sub>2</sub>/SiC coatings and rare-earth modified ZrB<sub>2</sub>/SiC coatings. Rare-earth oxides were incorporated into the coatings via mechanical mixing Sm<sub>2</sub>O<sub>3</sub> or Tm<sub>2</sub>O<sub>3</sub> with spray-dried ZrB<sub>2</sub>, or chemically doping samarium ions into spray-dried ZrB<sub>2</sub>. The SiC powders were mechanically mixed into the rare-earth modified ZrB<sub>2</sub> powders and the coatings were fabricated via shrouded air plasma spray. Following either a 30 or 60 s ablation test, coatings were evaluated with respect to their phase assemblage and microstructures. The baseline ZrB<sub>2</sub>/SiC coatings formed a porous and brittle  $m$ -ZrO<sub>2</sub> scale, which subsequently spalled from the unreacted coating during cooling. The rare-earth modified coatings, on the other hand, formed a protective scale composed primarily of  $c_1$ -Sm<sub>0.2</sub>Zr<sub>0.8</sub>O<sub>1.9</sub> or  $c_1$ -Tm<sub>0.2</sub>Zr<sub>0.8</sub>O<sub>1.9</sub>, depending on the starting coating composition, with a trace amount of  $m$ -ZrO<sub>2</sub>. These

$c_1$ -Sm<sub>0.2</sub>Zr<sub>0.8</sub>O<sub>1.9</sub> and  $c_1$ -Tm<sub>0.2</sub>Zr<sub>0.8</sub>O<sub>1.9</sub> oxide scales adhered well to the unreacted coatings during cooling. In summary, the effect of the rare-earth oxide and dopant additions is to stabilize the zirconia phase formed during oxidation into a more desirable compound than  $m$ -ZrO<sub>2</sub>. Coupling the high-temperature phase stability of  $c_1$ -Sm<sub>0.2</sub>Zr<sub>0.8</sub>O<sub>1.9</sub> with the high emissivity of Sm<sup>3+</sup> ions<sup>12,13,15</sup> may provide significant protection in hypersonic environments.

## Acknowledgments

The authors acknowledge the financial support from Dr. Ali Sayir of the Air Force Office of Scientific Research (AFOSR grant # FA9550-11-1-0079). The authors are also grateful for the assistance of Dr. Pablo Andres Gomez Florez from EPM, Colombia on the ablation torch setup and Praxair Surface Technologies for providing access to the plasma spray facilities.

## References

1. H. Squire and J. Marschall, "Material Property Requirements for Analysis and Design of UHTC Components in Hypersonic Applications," *J. Eur. Ceram. Soc.*, **30**, 2239–51 (2010).
2. A. Bongiorno, C. J. Först, R. K. Kalia, J. Li, J. Marschall, A. Nakano, M. M. Opeka, I. G. Talmy, P. Vashishta, and S. Yip, "A Perspective on Modeling Materials in Extreme Environments: Oxidation of Ultrahigh-Temperature Ceramics," *MRS Bull.*, **31**, 410–7 (2006).
3. N. Richet, P. Lespade, P. Goursat, and E. Laborde, "Oxidation Resistance of HfB<sub>2</sub>-SiC Coatings for Protection of Carbon Fiber Based Composites," *Key Eng. Mater.*, **264–268**, 1047–50 (2004).
4. E. Wuchina, E. Opila, M. Opeka, W. Fahrenholtz, and I. Talmy, "UHTCs: Ultra-High Temperature Ceramic Materials for Extreme Environment Applications," *Electrochem. Soc. Interface* [Winter] **16** [4] 30–6 (2007).
5. W. C. Tripp and H. C. Graham, "Thermogravimetric Study of the Oxidation of ZrB<sub>2</sub> in the Temperature Range of 800°C to 1500°C," *J. Electrochem. Soc.*, **118**, 1195–9 (1971).
6. A. Rezaie, W. G. Fahrenholtz, and G. E. Hilmas, "Evolution of Structure During the Oxidation of Zirconium Diboride-Silicon Carbide in air up to 1500°C," *J. Eur. Ceram. Soc.*, **27** [6] 2495–501 (2007).
7. S. C. Zhang, G. E. Hilmas, and W. G. Fahrenholtz, "Improved Oxidation Resistance of Zirconium Diboride by Tungsten Carbide Additions," *J. Am. Ceram. Soc.*, **91** [11] 3530–5 (2008).
8. F. Peng, Y. Berta, and R. F. Speyer, "Effect of SiC, TaB<sub>2</sub> and TaSi<sub>2</sub> Additives on the Isothermal Oxidation Resistance of Fully Dense Zirconium Diboride," *J. Mater. Res.*, **24** [5] 1855–67 (2009).
9. X.-H. Zhang, P. Hu, J.-C. Han, L. Xu, and S.-H. Meng, "The Addition of Lanthanum Hexaboride to Zirconium Diboride for Improved Oxidation Resistance," *Scripta Mater.*, **57**, 1036–9 (2007).
10. E. Opila, S. Levine, and J. Lorincz, "Oxidation of ZrB<sub>2</sub>- and HfB<sub>2</sub>-Based Ultra-High Temperature Ceramics: Effect of Ta Additions," *J. Mater. Sci.*, **39** [19] 5969–77 (2004).
11. D. M. Van Wie, D. G. Drewry, D. E. King, and C. M. Hudson, "The Hypersonic Environment: Required Operating Conditions and Design Challenges," *J. Mater. Sci.*, **39** [19] 5915–24 (2004).
12. G. E. Guazzoni, "High-Temperature Spectral Emission of Oxides of Erbium, Samarium, Neodymium and Ytterbium," *Appl. Spectrosc.*, **26** [1] 60–5 (1972).
13. W. R. McMahon and D. R. Wilder, "Hemispherical Spectral Emission of Selected Rare Earth Oxides," *J. Am. Ceram. Soc.*, **51** [4] 187–92 (1968).
14. S. M. Avdoshenko and A. Strachan, "High-Temperature Emissivity of Silica, Zirconia and Samaria From ab Initio Simulations: Role of Defects and Disorder," *J. Appl. Phys.*, accepted (2013).
15. W. Tan, C. A. Petorak, and R. W. Trice, "Rare-Earth Modified Zirconium Diboride High Emissivity Coatings for Hypersonic Applications," *J. Eur. Ceram. Soc.*, **34**, 1–11 (2014).
16. R. G. Munro, "Evaluated Material Properties for  $\alpha$ -Sintered Alumina," *J. Am. Ceram. Soc.*, **80** [8] 1919–28 (1997).
17. Metals and Ceramics Information Center, *Engineering Property Data on Selected Ceramics, Single Oxides*. Vol. III, Columbus Laboratories, Columbus, OH, (1981).
18. ASTM E 285-08, "Standard Test Method for Oxyacetylene Ablation Testing of Thermal Insulation Materials." ASTM International (2008).
19. ASTM C 373-88, "Standard Test Method for Water Absorption, Bulk Density, Apparent Porosity, and Apparent Specific Gravity of Fired White-ware Products." ASTM International (2006).
20. M. Tului, S. Lionetti, G. Pulci, E. Rocca, T. Valente, and G. Marino, "Effects of Heat Treatments on Oxidation Resistance and Mechanical Properties of Ultra High Temperature Ceramic Coatings," *Surf. Coat. Technol.*, **202** [18] 4394–8 (2008).
21. F. Monteverde, D. Alfano, and R. Savino, "Effects of LaB<sub>6</sub> Addition on Arc-Jet Convectively Heated SiC-Containing ZrB<sub>2</sub>-Based Ultra-High Temperature Ceramics in High Enthalpy Supersonic Airflows," *Corros. Sci.*, **75**, 444–53 (2013).
22. D. D. Jayaseelan, E. Zapata-Solvas, P. Brown, and W. E. Lee, "In Situ Formation of Oxidation Resistant Refractory Coatings on SiC-Reinforced ZrB<sub>2</sub> Ultra High Temperature Ceramics," *J. Am. Ceram. Soc.*, **95** [4] 1247–54 (2012).

<sup>23</sup>A. Rouanet, "Zirconium Dioxide-Lanthanide Oxide Systems Close to the Melting Point," *Rev. Int. Hautes Temp. Refract.*, **8** [2] 161–80 (1971).

<sup>24</sup>H. Yokokawa, N. Sakai, T. Kawada, and M. Dokiya, "Phase Diagram Calculations for ZrO<sub>2</sub> Based Ceramics: Thermodynamic Regularities in Zirconate Formation and Solubilities of Transition Metal Oxides"; pp. 59–68 in *Sci. Technol. Zirconia V*, [Int. Conf.], 5th, Edited by S. P. S. Badwal, M. J. Bannister, and R. H. J. Hannink. The Australian Ceramic Society, The Technomic Publication Co. Inc., Melbourne, Australia, August 16–21, 1993.

<sup>25</sup>W. G. Fahrenholtz, "Thermodynamic Analysis of ZrB<sub>2</sub>-SiC Oxidation: Formation of a SiC-Depleted Region," *J. Am. Ceram. Soc.*, **90** [1] 143–8 (2007).

<sup>26</sup>F. Monteverde, R. Savino, and M. D. S. Fumo, "Dynamic Oxidation of Ultra-High Temperature ZrB<sub>2</sub>-SiC Under High Enthalpy Supersonic Flows, 53, 922-29 (2011)," *Corros. Sci.*, **53**, 922–9 (2011).

<sup>27</sup>Z.-G. Liu, J.-H. Ouyang, B.-H. Wang, Y. Zhou, and J. Li, "Thermal Expansion and Thermal Conductivity of Sm<sub>x</sub>Zr<sub>1-x</sub>O<sub>2-x/2</sub> (0.1 ≤ x ≤ 0.5) Ceramics," *Ceram. Int.*, **35**, 791–6 (2009).

<sup>28</sup>W. M. Kriven, "Possible Alternative Transformation Tougheners to Zirconia: Crystallographic Aspects," *J. Am. Ceram. Soc.*, **72** [12] 1021–30 (1988). □